

BLDC Motor and Drive Conducted RFI Simulation for Automotive Applications

John E. Makaran, *Student Member, IEEE*, and Joe LoVetri, *Member, IEEE*

Abstract—In considering automotive conducted radio-frequency-interference (RFI) specifications applicable to motors and their associated drives, simulation of conducted RF emissions in the range from 150 kHz to 30 MHz is an area of interest from the product design perspective for several reasons. Traditionally, suppression of conducted noise in this frequency range of interest has been achieved through the use of bulk suppression elements such as capacitors and inductors. These elements consume valuable space within the motor, as well as add cost. The selection of bulk noise suppression elements, has, in the past, been predominately made through trial and error “brute force” methods. A method is presented whereby conducted RFI emissions can be simulated through the use of a high-fidelity virtual motor and drive model, as well as a virtual spectrum analyzer. Experimental validation of the model shows that accurate predictions can be made in the low-frequency range, below 10 MHz. Suggestions are made on how to improve the model at higher frequencies.

Index Terms—Brushless dc (BLDC), electromagnetic (EMC) simulation, fast Fourier transform (FFT), pulsewidth modulation (PWM), radio-frequency interference (RFI).

I. INTRODUCTION

IN RECENT YEARS, brushless dc (BLDC) motors have been introduced for engine cooling applications, replacing conventional belt driven and electrodrive cooling fans with one or two discrete speeds. In automobiles, the introduction of electronically commutated motors has been accompanied by a proliferation of electronic devices. With this proliferation of electronic devices, an emphasis has been placed on EMC issues. The increase in the capabilities of electronic simulation tools has resulted in the feasibility of modeling complete electromechanical systems. Through the use of analog behavioral modeling, the mechanical behavior of the motor and its associated load can be simulated using an electronics simulation package such as PSPICE. Such a model can be used not only to predict low-frequency phenomenon such as torque ripple, but can also be extended to the prediction of conducted RFI emissions.

The virtual motor model created in this study includes measured, lumped parameter models of the self inductance of the motor phases, as well as mutual coupling between the motor phases, iron losses, and the associated pulsewidth-modulated (PWM) drive and load. The parameters of the two motor windings studied are summarized in Table I.

TABLE I
SUMMARY OF RELEVANT MOTOR WINDING PARAMETERS

Motor Winding	Winding Resistance (m Ω)	Winding Inductance (μ H)	Fan Constant (rad s ⁻¹ /Nm ^{1/2})
10 Turns, 17 AWG	100	120	302.85
9 Turns, 18 AWG	90	111	336.50

Several pertinent papers have been published in recent years concerning the simulation of conducted RFI emissions in brushless motors [1]–[6] for industrial applications. All of these treat conducted emissions for high voltage, three phase, synchronous and asynchronous, bipolar motors for electric vehicles, or industrial applications. As such, there are no papers examining conducted RFI emissions from low-voltage, high-current, unipolar permanent magnet motors. This paper considers the simulation of conducted RFI emissions from a 13-V, 400-W, five-phase, permanent magnet, unipolar, BLDC motor for use in an underhood automotive engine cooling application. The frequency range of interest for this study ranges from 0.15 to 30 MHz. The techniques implemented in this research can be easily extended to other motor drive applications.

II. MODEL FORMULATION

A block diagram of the experimental setup that was modeled is shown in Fig. 1. The loading of the motor consists of the cooling fan associated with the application. The motor case is grounded to the negative control lead, which in turn is connected to the ground plane of the test setup, and the motor itself is placed on a 50-mm-thick insulator.

In this study, the conducted emissions are obtained during medium- and high-speed operation. The magnitude and frequency content of conducted RFI emissions in motors and drives is dominated by the magnitude and switching times of the motor current. As such, the system model must consider the interaction between the electrical, magnetic, and mechanical behavior of the motor and load. This relationship is represented in block diagram form in Fig. 2.

The electrical behavior of the machine is described by

$$\mathbf{v} = \mathbf{r}^T \mathbf{i} + \frac{d}{dt} [\mathbf{L}(\theta_r) \mathbf{i}] + d/dt \lambda_m(\theta_r) \quad (1)$$

in which the applied voltage vector, \mathbf{v} , represents the voltage applied to the terminals of the motor (V). In the case where PWM is used to control the speed of the motor, \mathbf{v} will be a function of the PWM duty cycle. At full speed, the motor terminals will see

Manuscript received March 22, 2002; revised January 7, 2003.

J. E. Makaran is with the Siemens VDO Automotive Inc., London, ON N6E 1R6, Canada.

J. LoVetri is with the Department of Electrical and Computer Engineering, University of Manitoba, Winnipeg, MB R3T 5V6, Canada.

Digital Object Identifier 10.1109/TEMC.2003.811304

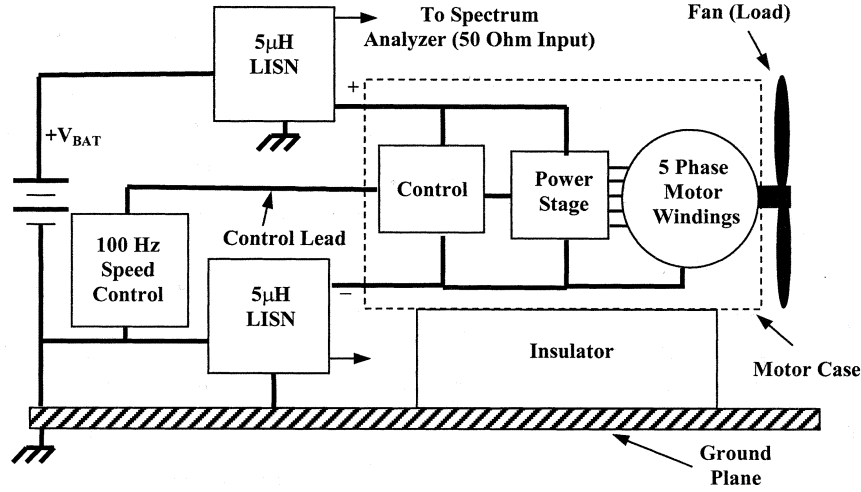


Fig. 1. Schematic representation of experimental test setup.

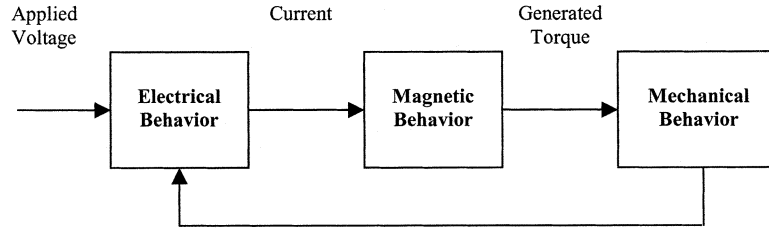


Fig. 2. Relationship between electrical, magnetic, and mechanical system behavior.

the full battery voltage (PWM duty cycle = 100%). The vector \mathbf{r} represents the dc resistance vector of the motor phases (Ω). The rotor position is represented by θ_r (rad). $\mathbf{L}(\theta_r)$ is the motor inductance matrix as a function of rotor position (H). The inductance matrix will include self and mutual inductance terms. The phase current vector is represented by \mathbf{i} (A), and $\lambda_m(\theta_r)$ is the flux vector with respect to the rotor position (Wb).

The magnetic behavior of the machine is governed by

$$T_e \frac{d\theta_r}{dt} = \left[\mathbf{i}^T \frac{d}{dt} \lambda_m(\theta_r) \right] \quad (2)$$

in which T_e (Nm) represents the generated electromagnetic torque.

The mechanical behavior of the machine can be described by

$$T_e = J \frac{d^2\theta_r}{dt^2} + B_m \frac{d\theta_r}{dt} + T_L \quad (3)$$

where J is the moment of inertia of the motor rotor and fan load (kg m^2), B_m represents the iron and damping losses of the motor (Nm s/rad), and T_L represents the motor load (Nm). For the case of a fan load, the torque is given as

$$T_L = \frac{\left(\frac{d\theta_r}{dt} \right)^2}{K_{\text{fan}}^2} \quad (4)$$

where the motor shaft speed is represented by $d\theta_r/dt$ (rad/s) while K_{fan} is the fan load constant ($\text{rad/s/Nm}^{1/2}$).

If the characterization of low-frequency motor performance is desired, (1)–(3) can be solved numerically. A numerical approach to solving these equations has been used in the past

to model low-frequency behavior of motors and their associated loads. The equations governing the behavior of a three phase synchronous machine under no-load conditions have been solved using the Runge–Kutta technique [7]–[10]. Similarly, the real-time simulations of induction motors have been performed. Some authors such as Strahan [11], Zhang *et al.* [12], Jack *et al.* [13], [14], and Cho [15] have studied motor performance via numerical solutions of these, or similar, differential equations. Typically, models based on the solution of such equations can be used to evaluate general electromechanical behavior but RFI concerns cannot be taken into account. This is due primarily to the difficulty of incorporating parasitic properties of the motor drive circuit elements into these equations. Work has been performed, however, on the use of state variable techniques to predict conducted emissions in switch-mode power supplies [16]. Parasitic capacitance and inductance on the boards in which the motor drives are implemented contribute greatly to the high-frequency conducted emissions. In the area of conducted RFI mitigation, measurement based techniques have been used to examine the effects of decoupling components across the power supply of printed circuit boards for frequencies up to 1 GHz [17].

Typically, publications dealing with brushless applications have examined the relationship between motor and drive for high voltage, three phase bipolar induction motors for use in electric vehicle or industrial applications. As such, there are no papers examining conducted RFI emissions from low-voltage, high-current, permanent magnet motors. In the prediction of conducted RFI emissions, the steady-state-system behavior

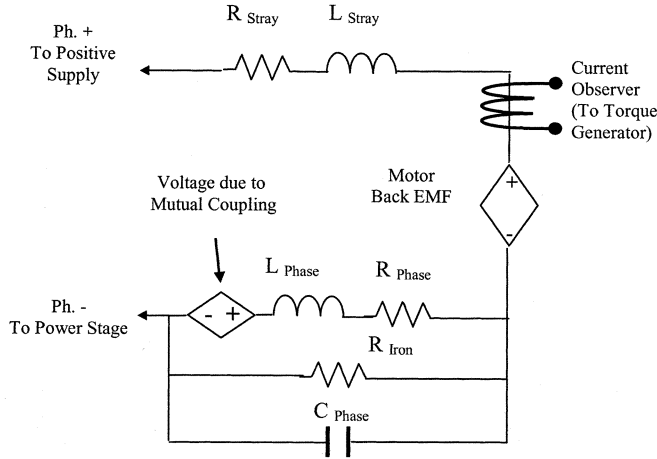


Fig. 3. Electrical model of a single motor phase.

under load conditions is of concern. For low-voltage, high-current applications, magnetic nonlinearities and switching device parasitics cannot be ignored.

To attempt to model the high-frequency behavior of the machine, drive, and associated load, a solution based on modifying the above equations is unwieldy for several reasons. The primary reason is the high number of energy-storage elements (capacitors and inductors) that are present in the motor and drive. These elements would add to the complexity of the set of differential equations. The equations could be simplified through various assumptions, however, the accuracy of the model would be compromised. To predict the conducted RFI behavior of the system in this frequency range of interest, bulk and parasitic elements of active and passive components in the inverter must be included. In order to include parasitic terms present in electronic components such as diodes and MOSFETs, the entire motor and drive system was simulated using lumped element modeling in SPICE.

III. SPICE ELECTRICAL-MOTOR MODEL

The magnetic behavior of the machine and the fan load were determined experimentally and incorporated in the model. As such, the magnetic model employed was a lumped, measured parameter model. All of the magnetic parameters such as the back EMF constants, self and mutual inductances were measured, but could have been predicted using numerical techniques such as a finite element method. Once the magnetic parameters were obtained, the magnetic behavior of the motor was adapted for the fan load across the entire operational speed range of the system. The complete model of one motor phase is shown in Fig. 3. The system was modeled omitting significant RFI suppression components in order to examine the contribution of the motor and drive to conducted RFI emissions.

Examining Fig. 3, the top of the motor phase is connected to the positive voltage supply. This connection in turn, is in series with a current controlled voltage source which is used as the phase current observer. This is in series with the phase back EMF, the phase self-inductance, and the phase winding resistance. The trapezoidal motor phase back EMF was modeled as a series of first, third, and fifth harmonics obtained

through measurements. At the bottom of the motor phase is a voltage source used to represent the sum of the mutually coupled voltages from the other motor phases. The individual mutually coupled voltage contributions incorporate the actual measured values of the mutual inductance between the phase of interest and the other motor phases. The expressions for mutual inductances as a function of rotor position were represented through harmonic decomposition obtained through direct measurement. A description of the dependent voltage sources used to model the mutual coupling is given below.

In parallel with the motor phase are the phase self capacitance, and the phase iron losses that were obtained using motor loss separation tests.

In a PWM motor drive, conducted RFI emissions at lower frequencies are influenced by the larger energy storage elements in the motor and drive, such as the motor phase inductance. As such, it was decided to measure the motor self and mutual inductances as a function of rotor position. Since the motor being studied is unipolar, only the part of the $B-H$ curve in the first quadrant is traversed during operation (i.e., current can only flow in one direction during one electrical cycle). In order to incorporate the effects of magnetic nonlinearities, it was decided not to use an LCR meter to measure the motor inductances. A method of experimentally determining the inductance that takes into account the magnetic behavior of the motor under various operating conditions is described as follows. The inductance, L , of an N -turn phase winding for any angular position, θ_r , can be written as

$$L(\theta_r) = \frac{\lambda(\theta_r)}{i} (H) \quad (5)$$

where $\lambda(\theta_r) = N\phi(\theta_r)$ (Wb) is the total flux linkage linking that phase at the angular position θ_r , and $i(A)$ is the current in the phase. The induced EMF in the phase winding may be written as

$$E(\theta_r) = -N \frac{d\phi(\theta_r)}{dt} (V). \quad (6)$$

Integrating the induced EMF with respect to time, the total flux linkage $\lambda(\theta_r)$ is obtained

$$\lambda(\theta_r) = \int_0^t E(\theta_r) dt (Wb). \quad (7)$$

Once the total flux linkage is determined, the inductance of the motor phase can be easily obtained. In our measurements, excitation of the motor phase to a desired magnitude of current was achieved through low-frequency switching of the motor phase (~ 0.5 Hz), and subsequent integration of the resultant EMF. The magnetic coupling between adjacent motor phases is analogous to the coupling present between the primary and secondary windings of a transformer. Therefore, the mutual coupling between adjacent motor phases was determined via the same method. This arrangement is outlined in Fig. 4. As may be seen, there are two separate integrators, one to determine the primary motor phase inductance, and one to determine the mutual coupling between two adjacent motor phases.

The determination of self and mutual inductance was performed at discrete angular positions across one mechanical pole

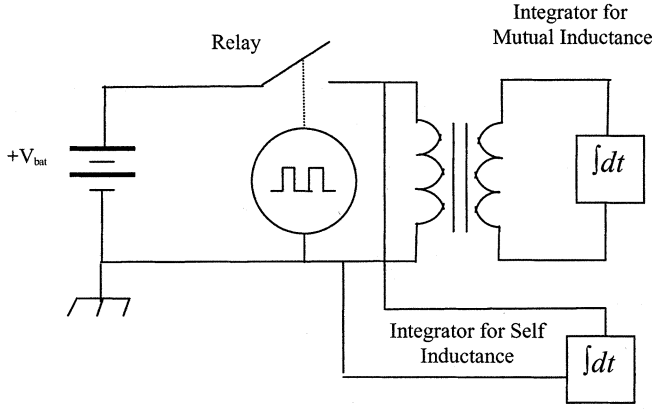


Fig. 4. Experimental setup to determine motor inductance matrix.

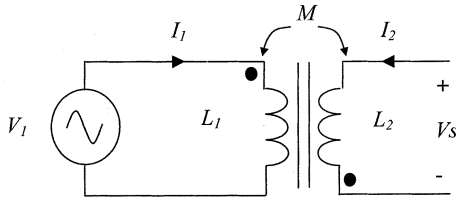


Fig. 5. Simple transformer model used in modeling of mutual coupling between motor phases.

pair to determine the inductance matrix as a function of rotor position. It was found that there was no significant change in the phase self inductances as a function of rotor position and these were, therefore, represented by constant values. The mutual inductances, however, were represented using discrete functions of the rotor position.

In considering the inclusion of mutual coupling terms in the PSPICE model for a five-phase motor, the mutual coupling, or transformer action, between phases was modeled using dependent voltage sources. Consider a simple transformer comprised of a primary and secondary winding as illustrated in Fig. 5. The primary and secondary windings L_1 and L_2 respectively, are assumed to be ideal and lossless. They are coupled together on a lossless iron core through a mutual inductance, M . The primary winding is connected to a voltage source. The voltage across the secondary of the transformer is represented as V_s .

Applying KVL to the voltage drops clockwise around the primary loop, we have

$$L_1 \frac{dI_1}{dt} - M \frac{dI_2}{dt} = V_1 \quad (8)$$

whereas in the secondary loop, going counterclockwise, we have

$$L_2 \frac{dI_2}{dt} - M \frac{dI_1}{dt} = V_s. \quad (9)$$

We can think of the two terms $-M(dI_1/dt)$ and $-M(dI_2/dt)$ as voltage source contributions from the opposite side of the transformer. These two equations can be manipulated to get

$$\begin{aligned} & L_1 \frac{dI_1}{dt} - \left(\frac{M}{L_2} \right) \left[V_s + M \frac{dI_1}{dt} \right] \\ &= L_1 \frac{dI_1}{dt} - \left(\frac{M}{L_2} \right) V_s - \left(\frac{M^2}{L_2} \right) \frac{dI_1}{dt} = V_1 \end{aligned} \quad (10)$$

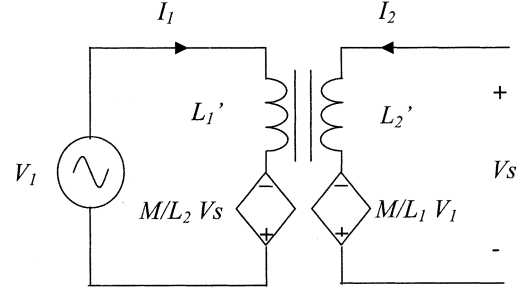


Fig. 6. Transformer model showing mutually coupled voltage terms as dependent voltage terms.

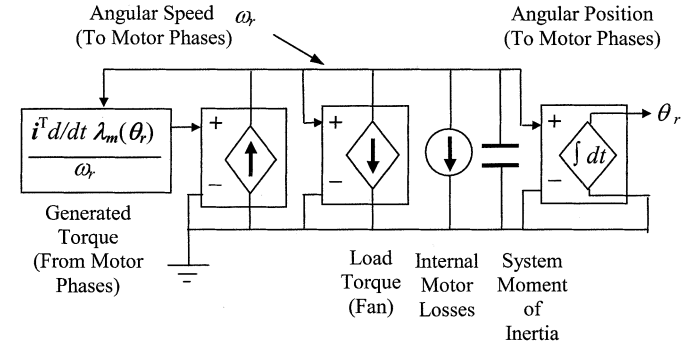


Fig. 7. Electromechanical motor model equivalent analog circuit representation.

$$\begin{aligned} & L_2 \frac{dI_2}{dt} - \left(\frac{M}{L_1} \right) \left[V_1 + M \frac{dI_2}{dt} \right] \\ &= L_2 \frac{dI_2}{dt} - \left(\frac{M}{L_1} \right) V_1 - \left(\frac{M^2}{L_1} \right) \frac{dI_2}{dt} = V_s. \end{aligned} \quad (11)$$

Writing the effective inductances as

$$L'_1 = L_1 - \left(\frac{M^2}{L_2} \right) \text{ and } L'_2 = L_2 - \left(\frac{M^2}{L_1} \right). \quad (12)$$

It is a simple matter to write the KVL equations as

$$L'_1 \frac{dI_1}{dt} - \left(\frac{M}{L_2} \right) V_s = V_1 \quad (13)$$

$$L'_2 \frac{dI_2}{dt} - \left(\frac{M}{L_1} \right) V_1 = V_s. \quad (14)$$

When the mutual coupling between the windings is weak, the coupling factor M is small, so the M^2 term is negligible and $L'_1 = L_1$ and $L'_2 = L_2$. Our exact (or approximate) transformer equations can now be implemented as dependent voltage controlled voltage sources as shown in Fig. 6.

By knowing the value of the mutual inductance as a function of rotor position, the voltage drop across the primary inductance, and the primary inductance as a function of rotor position, the mutual coupling between two motor phases can be modeled as a dependent voltage source.

IV. SPICE ELECTROMECHANICAL-MOTOR MODEL

In modeling the electromechanical motor model, the relationships in (2)–(4) had to be considered and incorporated into the SPICE model as a circuit element. Fundamentally, this was an exercise of modeling the various electromechanical torques as circuit elements.

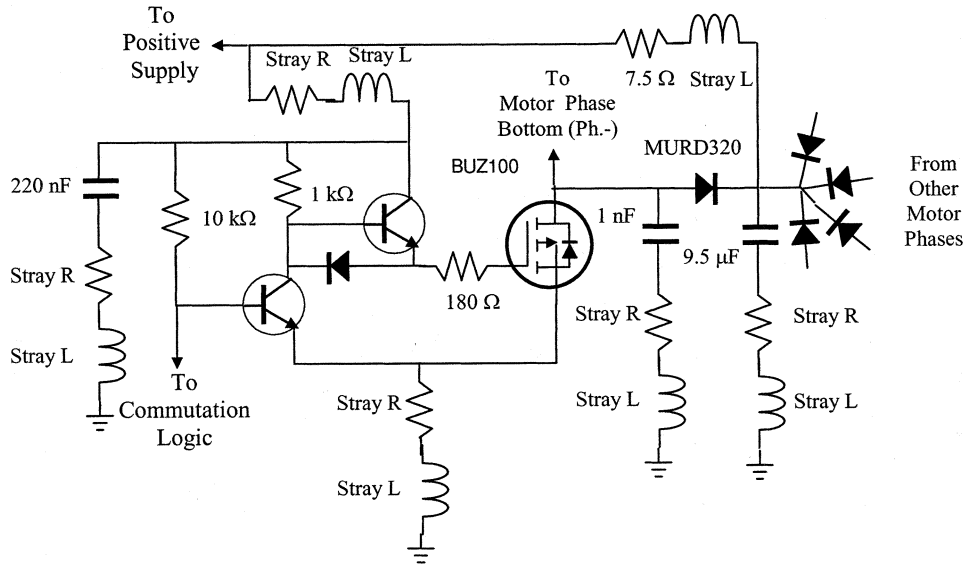


Fig. 8. Schematic representation of power stage of one motor phase.

Considering the first term of the right-hand side of (3) dealing with the torque contribution from the moment of inertia of the motor and fan, we write

$$T_{\text{Inertia}} = J \frac{d^2 \theta_r}{dt^2} \quad (15)$$

to

$$T_{\text{Inertia}} = J \frac{d\omega_r}{dt} \quad (16)$$

where ω_r is the angular velocity of the motor rotor (rad s^{-1}). This expression is analogous to the relationship governing the current through a capacitor $I = C dv/dt$. Hence, the moment of inertia of the motor and fan load may be represented as a capacitor, and the voltage across the capacitor may be used to represent the speed of the motor.

Combining (2), (3), and (4) yields

$$i^T \frac{d}{dt} \frac{\lambda m(\theta_r)}{\omega_r} = J \frac{d\omega_r}{dt} + B_m \omega_r + \frac{\omega_r^2}{K_{\text{fan}}^2}. \quad (17)$$

Thinking of this as a KCL equation, it is possible to represent (17) as a circuit with the various generated, loss, and load torques expressed as current sources. This circuit is illustrated schematically in Fig. 7. The motor speed is obtained by calculating the node voltage labeled ω_r in this circuit.

The voltage controlled current source used to represent the generated torque is comprised of the sum of the torques generated from each motor phase. The term representing the load torque is a voltage controlled current source incorporating the fan constant for the particular fan load. The internal motor loss torque, such as bearing friction, is modeled as a constant current source. Windage losses in this application were not significant, so they were excluded in the simulation model. The motor moment of inertia is modeled as a capacitor. Finally, the motor speed is integrated by a voltage controlled voltage source to obtain the angular position of the motor rotor. This information is then used to determine the phase back EMF and the mutual coupling between phases at that position.

V. POWER-STAGE MODELING

The model of the power stage which was used, for each phase, is shown in Fig. 8.

As may be seen in Fig. 8, the power stage of the motor is located on the low side of motor phase. The motor phases are energized by a BUZ100 MOSFET which, in turn, is energized by a totem pole MOSFET driver connected to the gate of the MOSFET. The MOSFET driver is bypassed with a 220 nF capacitor, while the MOSFET is bypassed with a 1 nF capacitor connected to the drain of the MOSFET to act as a turn-off switching aid. The freewheeling path for the coils is through the resistor, capacitor, diode (RCD) snubber comprised of the 7.5-Ω resistor, the 9.5-μF capacitor, and the MURD320 diode. The RCD snubber is shared by all five phases of the motor. The top of the 7.5-Ω resistor is connected to the positive voltage supply of the motor.

All active components were modeled using PSPICE equivalents from the appropriate manufacturers' libraries. Capacitors were modeled using their high-frequency model approximations including the appropriate values of lead inductance and equivalent series resistance from derived component data sheets. Printed-circuit-board (PCB) interconnections for high-current paths were modeled as series combinations of stray resistances and inductances. Consequently, the effects of capacitive or inductive coupling of noise from one PCB layer to another, or from one trace to another were ignored. The stray PCB resistances and inductances were obtained via measurements, and varied between phases. The decision to exclude the effects of capacitive and inductive coupling in the power stage model was made to simplify the model and to reduce computing time.

VI. LISN MODELING

The schematic for the line-impedance stabilization network (LISN) that was used in the measuring of conducted RFI emissions appears in Fig. 9. The LISN is a typical 5-μH LISN that

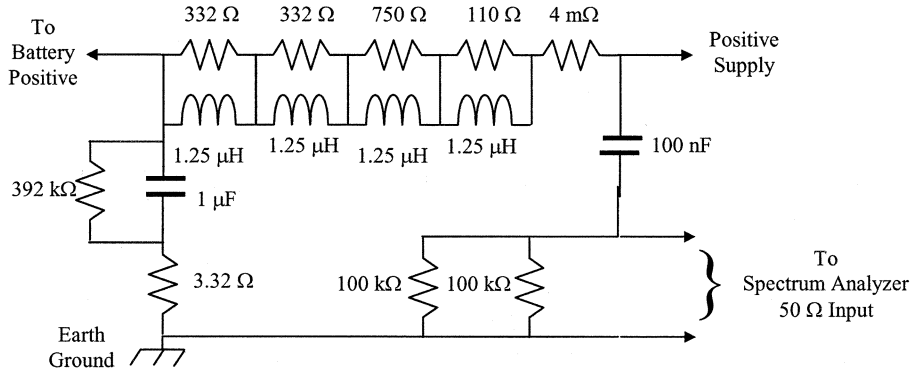


Fig. 9. Schematic representation of LISN.

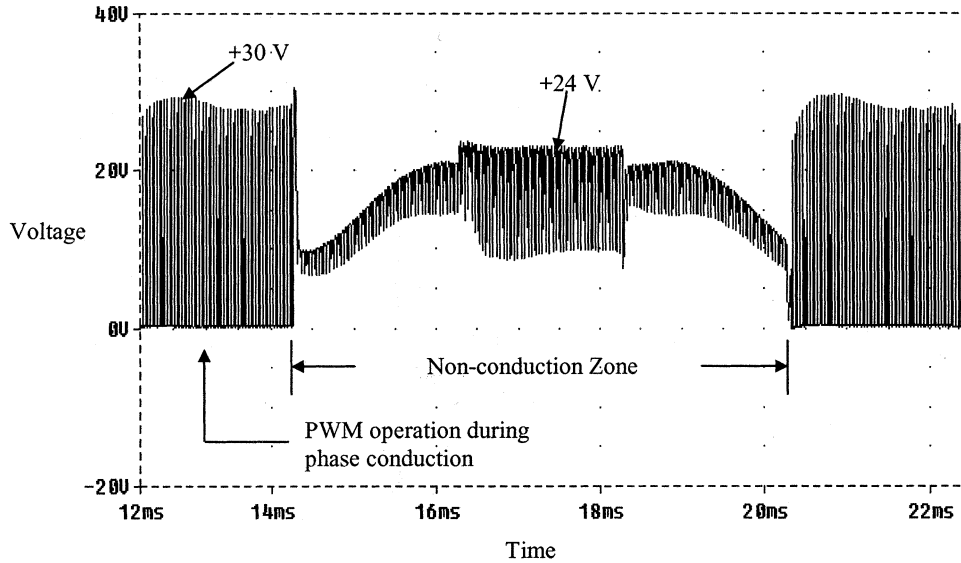


Fig. 10. Simulated MOSFET drain-to-source voltage at midspeed.

was placed in series with the positive supply of the motor. In accordance with the measurement set up, as governed by the conducted RFI specification which was used (a CISPR25 variant), an identical LISN was placed in series between the battery negative and the negative supply of the motor.

In the conducted RFI specification used in this study, limits are only placed on the differential mode noise; there was no requirement to measure common mode noise. Therefore, the modeling of sources of common mode emissions was not dealt with. In order to obtain the spectrum of the differential mode emissions, the time-domain LISN voltages were obtained through simulation and subsequently subjected to spectral analysis.

VII. TIME-DOMAIN RESULTS

Conducted emissions testing and simulations were performed and compared at a constant midspeed and constant high-speed. In the case of the nine-turn winding, this corresponds to speeds of 2200 rpm, and 2800 rpm, respectively. In the case of the ten-turn winding, this corresponds to speeds of 2000 and 2600 rpm, respectively.

Although the ultimate goal is to achieve frequency-domain data, time-domain results provide a valuable qualitative validation of the system model. Fig. 10 illustrates the simulated

drain-to-source voltage of one motor phase during midspeed operation, while, Fig. 11 illustrates the actual drain-to-source voltage of one motor phase during midspeed operation for a motor using the ten-turn winding.

Similarly, the simulated MOSFET drain-to-source voltage for a phase MOSFET appears in Fig. 12, while the measured MOSFET drain-to-source voltage appears in Fig. 13 for high-speed operation for a motor using the ten-turn winding.

As illustrated in the drain-to-source voltage waveforms, a “block” commutation control scheme is employed. In this scheme, the motor phase conducts for a defined period of time when the back EMF in the motor phase is greater than zero, and nonconducting for the remainder of the period. In Figs. 9 and 10, during midspeed operation, PWM is used to control the voltage across, and hence the current through, the motor windings during the conduction period of the motor phase. This is not the case during high-speed operation, where the full battery voltage is switched across the motor windings without PWM during the conduction period of the motor phase. As such, conducted emissions during midspeed operation are more problematic. It is worthy to note that the typical switching times for the MOSFET drain-to-source voltage during PWM are equal to approximately 1 μ s. The switching times of the

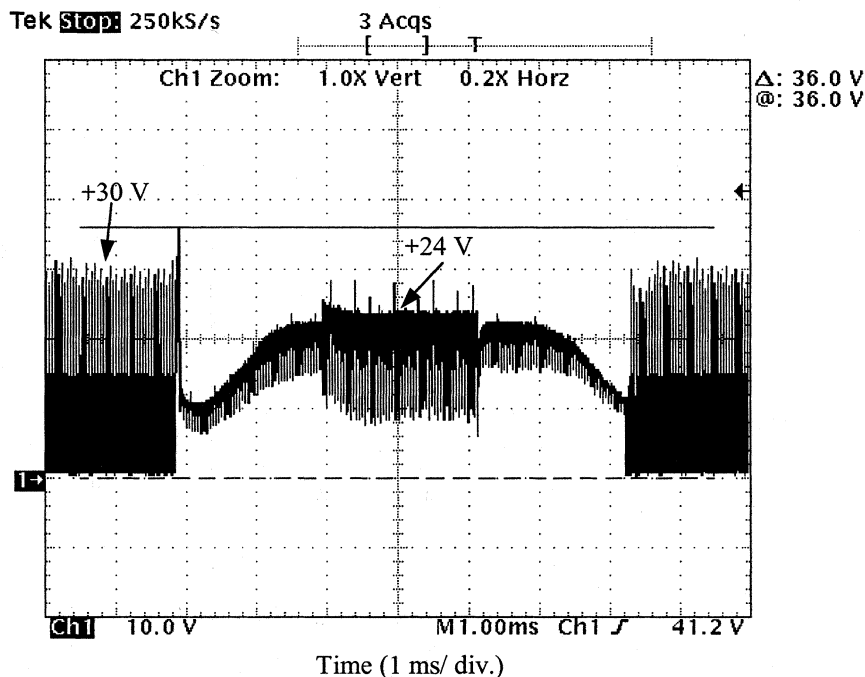


Fig. 11. Measured MOSFET drain-to-source voltage at midspeed.

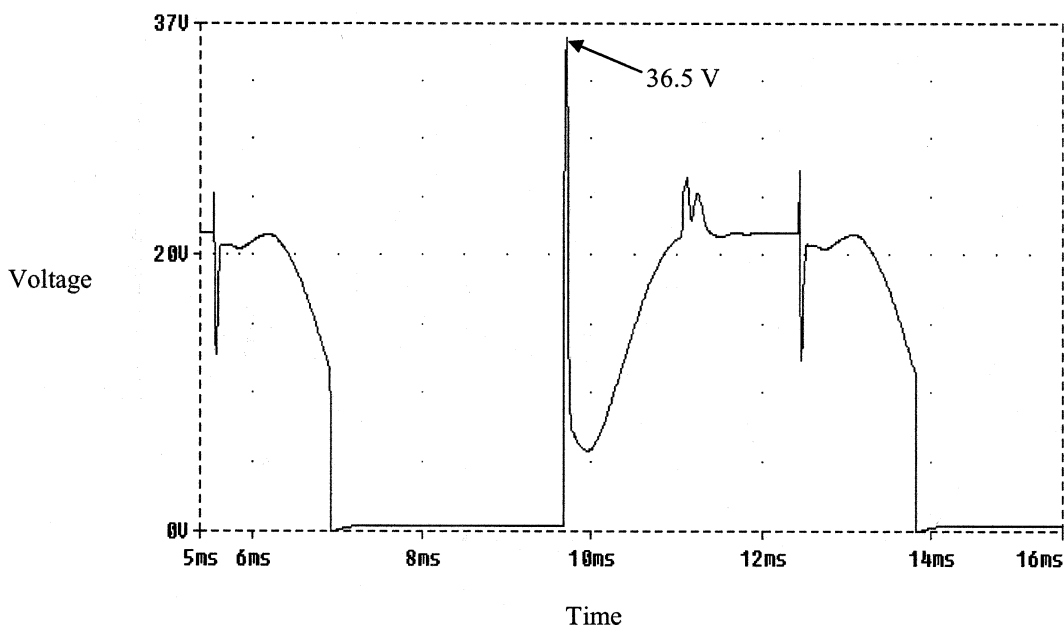


Fig. 12. Simulated MOSFET drain-to-source voltage at high speed.

microcontroller used to control the MOSFET drivers is considerably faster, between 150 and 200 ns. In both the simulated and measured cases for midspeed and high-speed operation the effects of mutual coupling from adjacent motor phases may be seen during the nonconducting period of a motor phase.

Examining Figs. 10–13, we see that the simulated and measured results show good comparison.

To compare the simulated and measured LISN voltages, the voltage at the output of the positive LISN was selected. The simulated positive LISN voltage for a motor operating at midspeed is shown in Fig. 14, while the measured positive LISN voltage

for midspeed conditions is shown in Fig. 15 for a motor using a ten-turn winding.

As may be seen in the waveforms for the midspeed case, the comparison between simulated and experimental waveforms is good both in terms of magnitude as well as shape. The maximum positive voltage of the conduction envelope in the simulated case is 66.7 mV which compares well with the measured value of 70.4 mV. The maximum negative voltage of the conduction envelope in the simulated case is -24.9 mV, which also compare well with the measured value of -22.0 mV. The envelope for the LISN voltage during one

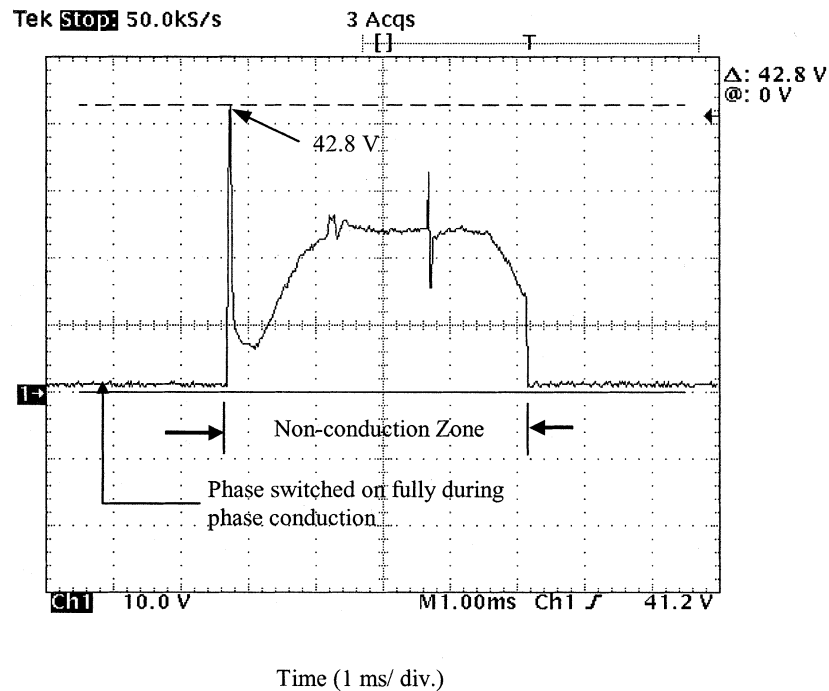


Fig. 13. Measured MOSFET drain-to-source voltage at high speed.

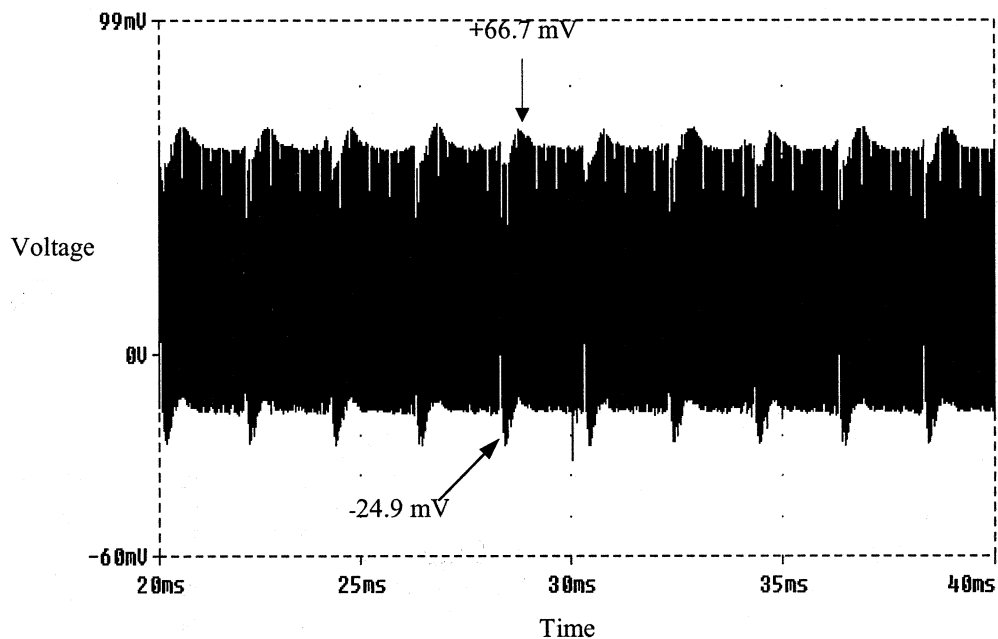


Fig. 14. Simulated LISN voltage at midspeed.

electrical cycle is the same in both the simulated and measured case.

The simulated positive LISN voltage at high speed is shown in Fig. 16. The measured positive LISN voltage for high-speed operation is shown in Fig. 17. In comparing the two cases, it may be seen that there is also good correlation between the simulated and measured cases. The large periodic peak in the waveform is the result of the behavior of the motor and drive during the transition of one motor phase turning off, to the turning on of the next motor phase in the commutation sequence. In the sim-

ulated case, the magnitude of this peak is equal to +63.5 mV, which compares well with the measured value of approximately +62 mV. The maximum negative voltage in the simulated case is equal to -24.6 mV, while in the measured case, the maximum negative voltage is equal to -24.8 mV. As such, in terms of the magnitude of the LISN voltages, there is good comparison between the simulated and measured results.

Once the time-domain LISN voltages were obtained, a method of determining the frequency spectrum of the LISN voltages was implemented.

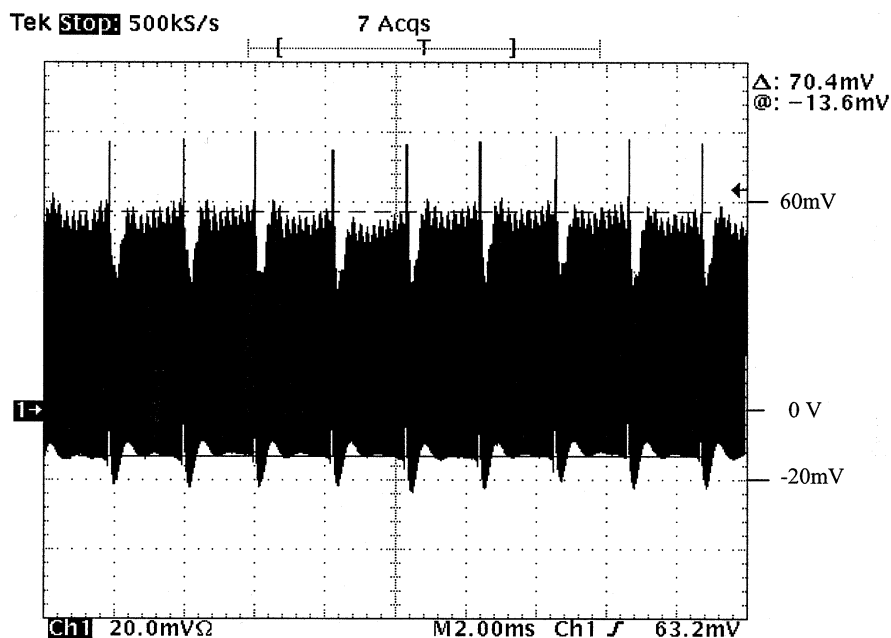


Fig. 15. Measured LISN voltage at midspeed.

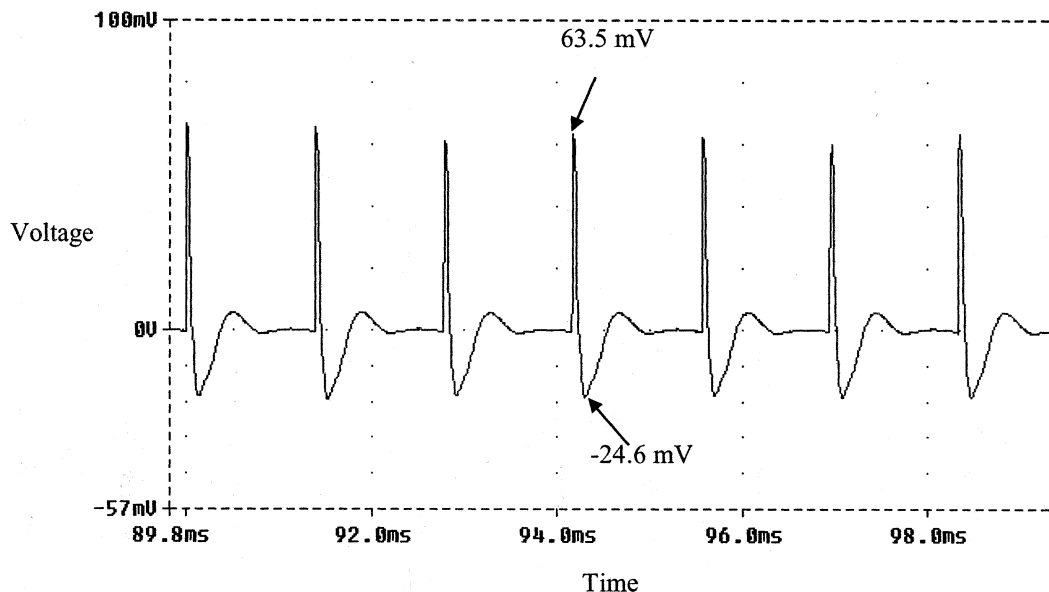


Fig. 16. Simulated LISN voltage at high speed.

VIII. DETERMINATION OF CONDUCTED RFI SPECTRUM

To obtain simulation results that could be correlated directly to measured results, it was decided to simulate the behavior of a typical superheterodyne spectrum analyzer which might be used in a conducted RFI measurement. The spectrum analyzer parameters that were duplicated in the MATLAB® simulation were obtained from a modified version of the CISPR 25 specification. The measurement parameters included an IF bandwidth of 10 kHz, frequency steps of 7.5 kHz, as well as peak detection with no attenuation.

To completely duplicate a superheterodyne type spectrum analyzer in PSPICE would be impractical due to long computing

times. Only the important features of a spectrum analyzer were modeled.

Two methods were attempted to implement the spectrum analyzer in MATLAB. The first method involved the implementation of a digital bandpass filter, whose characteristics approximated those of the IF filter of the actual spectrum analyzer. The center of the filter was swept across the frequency band of interest in discrete frequency steps. The digital filter was applied to the LISN time-domain voltage waveforms output from PSPICE for each frequency step.

In the duplication of the IF filter characteristics, a third order, digital, butterworth filter was used to simulate the steep roll-off characteristics of the IF filter. Although this method yielded the

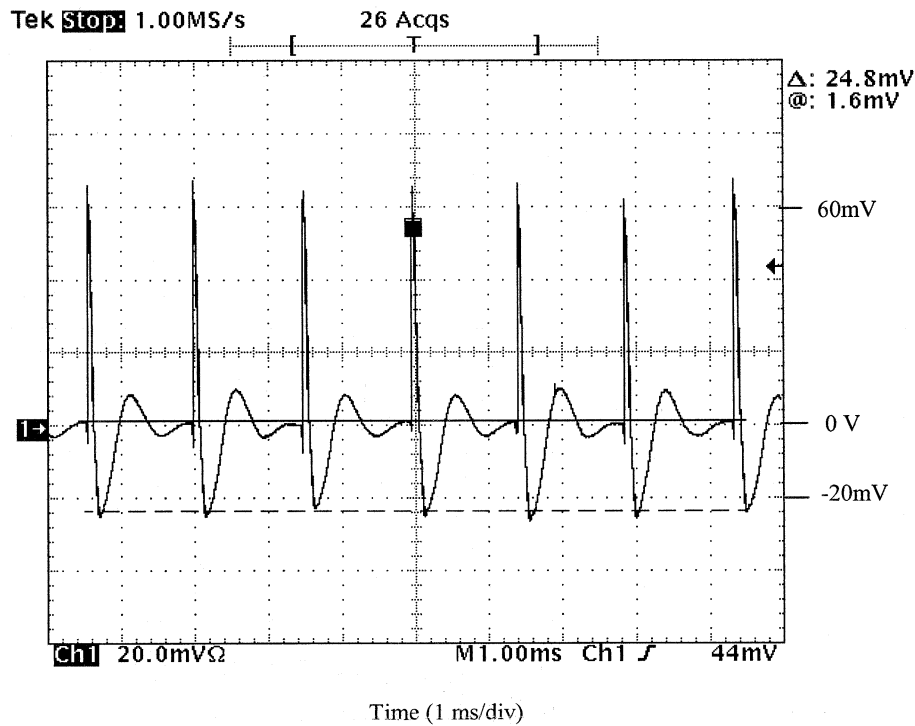


Fig. 17. Measured LISN voltage at high speed.

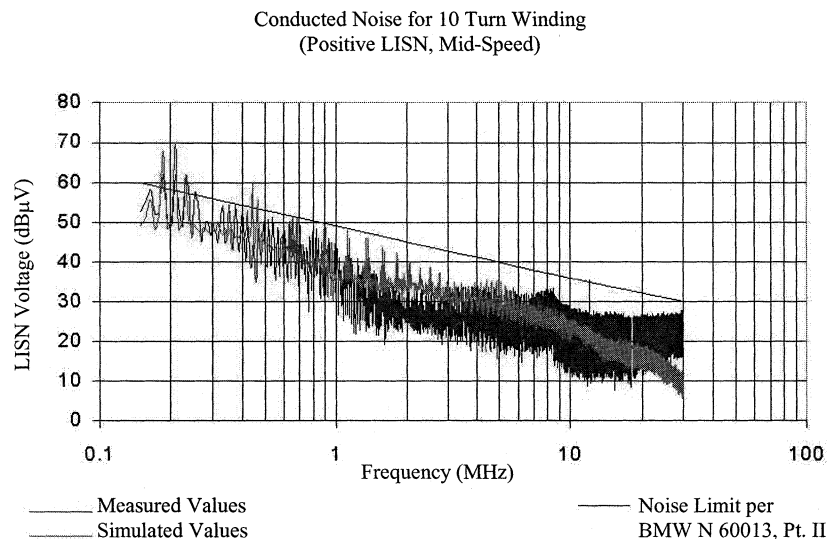


Fig. 18. Midspeed conducted RFI spectrum. (Ten turns, 17 AWG.)

most accurate results, this method was computationally intensive for a simple reason. According to Nyquist's criterion, the sampling frequency of a signal must be at least two times the frequency of interest. In applying the digital filter to the signal, as the frequency of interest increased, so too did the sampling frequency.

The second method that was implemented was to pass a sliding window over the time-domain data and apply a fast Fourier transform (FFT) to the windowed data. The FFT was performed for each window over the entire frequency range of interest at fixed frequency steps. In this case the conducted RFI was calculated every 7.5 kHz, from 150 kHz to 1 MHz.

To simulate a "peak hold" function of the spectrum analyzer, the FFT values for each window were subsequently compared, and the maximum value of the transform was kept for the particular frequency of interest. The FFT was performed using a Hamming window.

In terms of duplicating the characteristics of the IF filter using this method, the FFT was performed using the 10 kHz resolution bandwidth specified. As the filter characteristics of the IF filter in the spectrum analyzer used in experimental measurements possessed a steep roll-off, the shape of the peaks in the simulation were a good approximation for the characteristics of the IF filter used in experimental measurements.

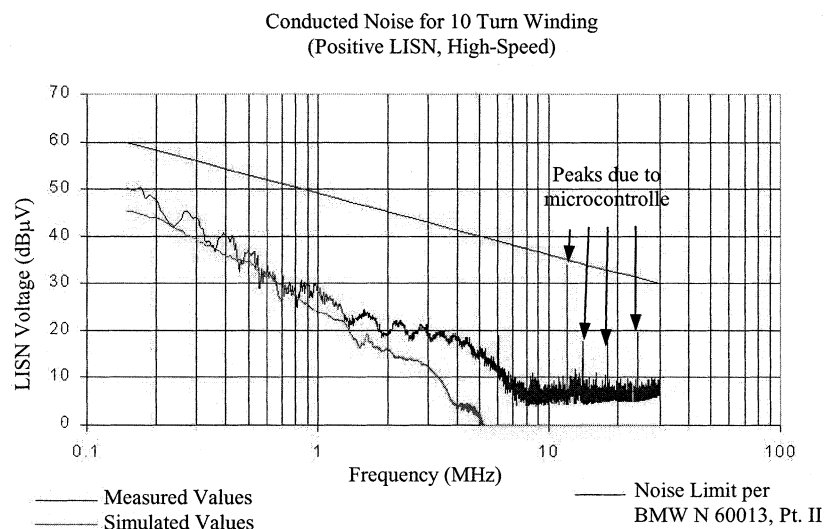


Fig. 19. High-speed conducted RFI spectrum. (Ten turns, 17 AWG.)

TABLE II
SUMMARY OF ERROR BETWEEN EXPERIMENTAL AND SIMULATED CONDUCTED RESULTS FOR MID-SPEED OPERATION. (TEN-TURN, 17-AWG WINDING)

Frequency Range	Average Difference (dB)	Worst Case Maximum Difference (dB)	Worst Case Minimum Difference (dB)
0.15 – 1 MHz	-0.608	11.908 at 0.68251 MHz	-16.926 at 0.88501 MHz
1 – 10 MHz	-3.491	8.941 at 8.078 MHz	-23.145 at 1.35001 MHz
10 – 30 MHz	4.516	20.26 at 29.6553 MHz	-14.27 at 10.1401 MHz

TABLE III
SUMMARY OF ERROR BETWEEN EXPERIMENTAL AND SIMULATED CONDUCTED RESULTS FOR HIGH-SPEED OPERATION. (TEN-TURN, 17-AWG WINDING)

Frequency Range	Average Difference (dB)	Worst Case Maximum Difference (dB)	Worst Case Minimum Difference (dB)
0.15 – 1 MHz	+1.89	5.74 at 0.97501 MHz	-3.26 at 0.69001 MHz
1 – 10 MHz	+8.45	18.8 at 6.03006 MHz	0.28 at 1.29751 MHz
10 – 30 MHz	+6.47	34 at 12.06012 MHz	4.22 at 14.60265 MHz

IX. FREQUENCY DOMAIN RESULTS

The FFT results for midspeed operation, and high-speed operation for the motor and drive without RFI suppression components appear in Figs. 18 and 19 for the ten-turn, 17-AWG motor winding, respectively. The straight line passing through the data on all graphs is the specification limit for the frequency range of interest. The darker curves on both graphs are the measured results. Tables II and III are a summary of the average and worst case errors between simulation and measurement in the mid-speed and high-speed case respectively for the ten-turn winding.

The midspeed results for the ten-turn, 17-AWG motor winding, show that the simulated values follow the same trend as the experimental values across the lower frequency

range of interest, however, the peak measurements obtained in the simulation are higher than the measured case. The difference between simulated and measured results increases at frequencies above 10 MHz. The discrepancies are attributable to several factors. Some discrepancy in the frequency-domain magnitudes at low frequencies may be due to the inherent differences between the FFT method used in simulation, and experimental measurement. One discrepancy may have to do with the characteristics of the spectrum analyzer peak detector used in measurement. At the higher frequencies, the discrepancy may be due to the absence of capacitive and inductive coupling between the PCB layers, or from the motor windings to the PCB, or from the PCB to the motor leads.

In the case of high-speed motor operation, the measured and simulated results show better comparison at lower frequencies, with the worst case difference equal to approximately 5.74 dB. The high-speed simulation results appear to be more broadband in nature than the experimental results, decreasing at approximately 20 dB per decade.

At frequencies greater than 1 MHz, however, the comparison between the simulated and measured results grows progressively larger, until the simulated conducted noise falls to zero at approximately 5 MHz. In addition, because the simulation model included a simplified model for the microcontroller used in the motor controller, at frequencies greater than 10 MHz the peaks due to the microcontroller oscillator harmonics that show up in the measured results of Fig. 19 are not evident in the simulation results. Despite the peaks due to the microcontroller resonator harmonics, the conducted noise in the measured results between 10 and 30 MHz remains largely at the noise floor of the measuring equipment. Clearly, at high-speed operation, the contribution of the motor as a source of conducted noise is negligible in this frequency range.

In examining the conducted noise results between 1 and 10 MHz for the high-speed case, it was also concluded that the difference in the simulated and measured results was due to the absence of a microcontroller model in the simulations. The MOSFET drivers in the application are controlled using a

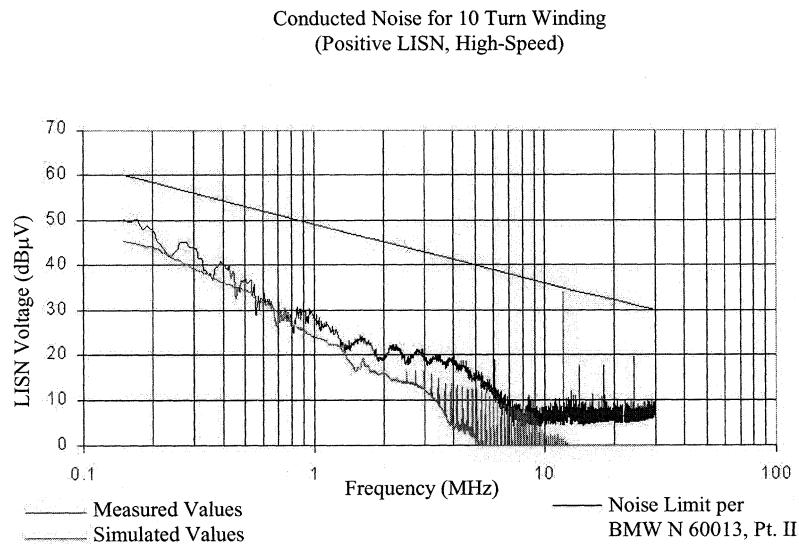


Fig. 20. High-speed conducted RFI spectrum including behavior of microcontroller. (Ten turns, 17 AWG.)

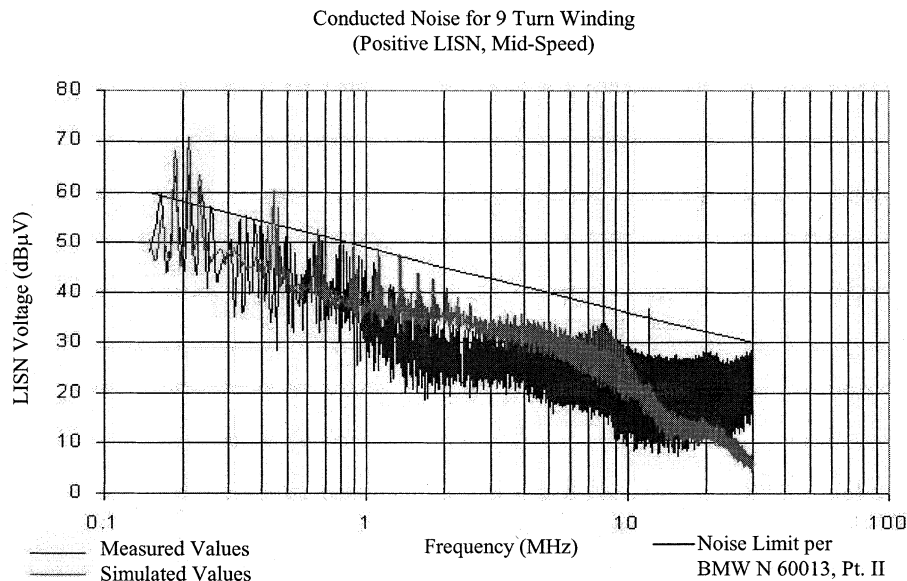


Fig. 21. Midspeed conducted RFI spectrum. (Nine turns, 18 AWG.)

compare timer output timer from a microcontroller that delivers the appropriate PWM signal to the inputs of the MOSFET drivers. For high-speed motor operation it is desired to operate the motor without PWM operation by switching the input to the MOSFET driver fully on. In the actual motor drive, however, the compare timer is not capable of turning the output of the microcontroller connected to the input of the MOSFET driver fully on. As a result, there is a 166.7 ns pulse appearing at the input of the MOSFET driver. Due to the time constants associated with the MOSFET driver, this 166.67 ns pulse does not affect the power stage of the motor phase, and as such, the motor phase is turned fully on during high-speed operation. This 166.7 ns pulse, however, is a significant noise source affecting the conducted noise spectrum of the motor.

In the simulation model for high-speed operation, the actual behavior of the microcontroller was originally omitted. Fig. 20 illustrates the conducted noise spectrum for the ten-turn winding

for high-speed operation once the actual behavior of the microcontroller was included. As may be seen in Fig. 20, once this noise source is included, the simulation results compare well to the measured results.

The midspeed and high-speed results for the nine-turn, 18-AWG winding appear in Figs. 21 and 22, respectively. Tables IV and V are a summary of the average and worst case errors between simulation and measurement in the midspeed and high-speed case, respectively, for the nine-turn winding.

In examining the conducted noise results in Fig. 21 for the nine-turn winding, the same trends in conducted noise for medium speed operation are observed as with the ten-turn winding.

The same may be said of the conducted noise results for the high-speed case for the nine-turn winding illustrated in Fig. 22. In making this observation, it is shown that the model is capable of predicting conducted noise using different motor windings.

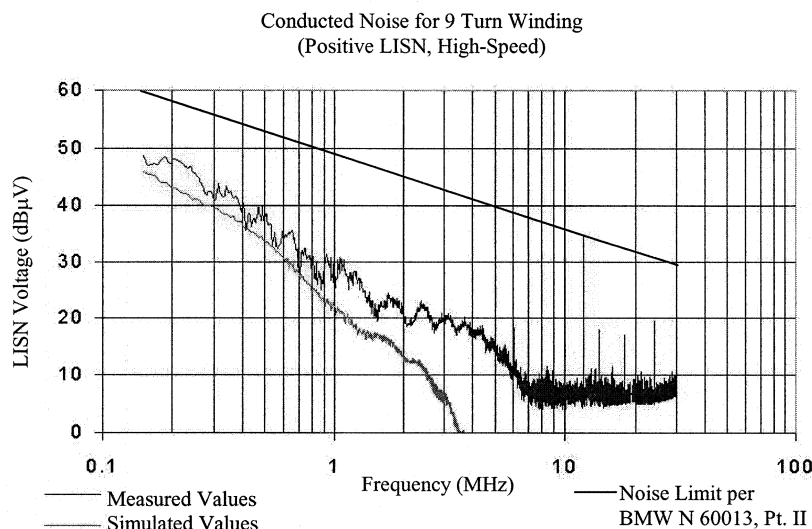


Fig. 22. High-speed conducted RFI spectrum. (Nine turns, 18 AWG.)

TABLE IV

SUMMARY OF ERROR BETWEEN EXPERIMENTAL AND SIMULATED CONDUCTED RESULTS FOR MID-SPEED OPERATION. (NINE-TURN, 18-AWG WINDING.)

Frequency Range	Average Difference (dB)	Worst Case Maximum Difference (dB)	Worst Case Minimum Difference (dB)
0.15 – 1 MHz	-0.347	11.324 at 0.80251 MHz	-19.07 at 0.93001 MHz
1 – 10 MHz	-4.383	11.63 at 8.13008 MHz	-24.013 at 1.11751 MHz
10 – 30 MHz	8.35	23.42 at 29.8578 MHz	-12.88 at 10.1401 MHz

TABLE V

SUMMARY OF ERROR BETWEEN EXPERIMENTAL AND SIMULATED CONDUCTED RESULTS FOR MID-SPEED OPERATION. (NINE-TURN, 18-AWG WINDING.)

Frequency Range	Average Difference (dB)	Worst Case Maximum Difference (dB)	Worst Case Minimum Difference (dB)
0.15 – 1 MHz	-3.88	8.03 at 0.92251 MHz	-1.38 at 0.69751 MHz
1 – 10 MHz	-10.247	20.2 at 3.69004 MHz	-1.00501 at 2.40221 MHz
10 – 30 MHz	6.7	34.17 at 12.06762 MHz	-4.35 at 10.1551 MHz

X. CONCLUSIONS

From the time-domain results, one may conclude that using a lumped parameter measured model is an effective method of predicting the time-domain LISN voltages from which a conducted RFI spectrum may be obtained.

As far as frequency-domain results are concerned, the correlation between simulated and experimental results show a few differences. The simulated results follow the general trend of the experimental results. The discrepancies may be attributable in part, to the methods used to model various motor parameters, and differences between the simulated and experimental methods used to obtain the frequency spectrum.

For example, the phase back EMFs were modeled as the sum of sinusoidal harmonic voltages. In reality, the phase back EMFs are a function of the flux in the air gap. It may be more prudent to use a finite element program to determine the flux in the air gap under the load conditions of concern so as to incorporate the effects of armature reaction on the shape of the phase back EMFs. Finite element tools could also be used to predict the values in the self and mutual inductance matrix, as well as iron losses.

At frequencies above 10 MHz, however, the difference between simulated and measured results is suspected to be caused by the absence in the model of parasitic coupling elements distributed across the various PCB layers.

Despite the differences between simulated and measured results, it can be concluded that this method of predicting conducted RFI emissions over the frequency range of interest can serve as a valuable simulation tool that can shorten the development cycle.

In this study, simulation has only been conducted on two motor windings with two different fan loads to frequencies of 30 MHz. It can be argued, through a more thorough characterization of stray PCB elements, and through the inclusion of capacitive and inductive coupling elements, the accuracy of the model could be improved at frequencies between 10 and 30 MHz, or higher. At the present time, to further validate the model the current motor windings with additional RFI suppression components are being evaluated. In addition, the conducted noise model is being further refined to 30 MHz through the inclusion of additional parasitic PCB trace impedances.

REFERENCES

- [1] E. Zhong and T. A. Lipo, "Improvements in EMC performance of inverter-fed motor drives," *IEEE Trans. Ind. Applicat.*, vol. 31, pp. 1247–1256, Nov. 1995.
- [2] G. Grandi, D. Casadei, and U. Reggiani, "Analysis of common- and differential-mode HF current components in PWM inverter-fed AC motors," in *Rec. 29th Annual Power Electronics Specialist Conf., PESC'98*, May 1998, pp. 1146–1151.

- [3] C. Chen and X. Xu, "Modeling the conducted EMI emission of an electric vehicle (EV) traction drive," in *Proc. IEEE Int. Symp. Electromagnetic Compatibility*, vol. 2, Aug. 1998, pp. 796–801.
- [4] L. Ran, S. Gokani, and J. Clare, "Conducted electromagnetic emissions in induction motor drive systems Part I: Time-domain analysis and identification of dominant modes," *IEEE Trans. Power Electron.*, vol. 13, pp. 757–767, July 1998.
- [5] —, "Conducted electromagnetic emissions in induction motor drive systems Part II: Frequency domain models," *IEEE Trans. Power Electron.*, vol. 13, pp. 768–775, July 1998.
- [6] H. Zhu, J.-S. Lai, A. R. Hefner, Y. Tang, and C. Chen, "Analysis of conducted EMI emissions from PWM inverter based on empirical models and comparative experiments," in *Proc. IEEE Power Electronics Specialist Conf., PESC'99*, vol. 2, 1999, pp. 861–867.
- [7] R. Spee and A. K. Wallace, "Performance characteristics of brushless DC drives," *IEEE Trans. Ind. Applicat.*, vol. 24, pp. 568–573, July 1988.
- [8] A. K. Wallace and R. Spee, "The effects of motor parameters on the performance of brushless DC drives," *IEEE Trans. Power Electron.*, vol. 5, pp. 2–8, Jan. 1990.
- [9] —, "The simulation of brushless DC drive failures," in *Proc. IEEE Power Electronics Specialist Conf., PESC'88*, vol. 1, Apr. 1988, pp. 199–206.
- [10] R. Spee and A. K. Wallace, "Performance characterization of brushless DC drives," in *Proc. IEEE IAS'87*, vol. 1, 1987, pp. 1–6.
- [11] R. J. Strahan, "Energy conversion by nonlinear permanent magnet machines," *Proc. Inst. Elect. Eng. Elect. Power Applicat.*, vol. 145, no. 3, pp. 103–198, 1998.
- [12] J. Zhang, R. Mathew, F. Flinders, and W. Oghanna, "Simulator of DC traction motors including both main and interpole saturation," *Proc. Inst. Elect. Eng. Elect. Power Applicat.*, vol. 145, no. 4, pp. 377–382, 1998.
- [13] A. G. Jack, D. J. Atkinson, and H. J. Slater, "Real-time emulation for power equipment development. Part 1: Real time simulation," *Proc. Inst. Elect. Eng. Elect. Power Applicat.*, vol. 145, no. 2, pp. 92–97, 1998.
- [14] —, "Real-time emulation for power equipment development. Part 2: Real time simulation," *Proc. Inst. Elect. Eng. Elect. Power Applicat.*, vol. 145, no. 2, pp. 153–158, 1998.
- [15] D.-H. Cho and K. Kim, "Modeling of electromagnetic excitation forces of small induction motor for vibration and noise analysis," *Proc. Inst. Elect. Eng. Elect. Power Applicat.*, vol. 145, no. 3, pp. 199–205, 1998.
- [16] R. Popescu, J. Roudet, and J.-C. Crebier, "Power electronic converter EMC analysis through state variable approach techniques," *IEEE Trans. Electromagn. Compat.*, vol. 43, pp. 229–238, May 2001.
- [17] T. Hubing, J. Drewniak, T. P. Van Doren, and D. M. Hockanson, "Power bus decoupling on multilayer printed circuit boards," *IEEE Trans. Electromagn. Compat.*, vol. 37, pp. 155–166, May 1995.
- [18] C. D. McGillem and G. R. Cooper, *Continuous and Discrete Signal and System Analysis*, 2nd ed. Toronto, Canada: Holt Rinehart & Winston, 1984.
- [19] C. K. Taft *et al.*, *Brushless Motor System Design and Analysis*, 11th ed. Durham, NH: Univ. New Hampshire Press, 1997.

John E. Makaran (S'87) was born in London, ON, Canada, in 1964. He received the B.E.Sc. degree in electrical engineering, the M.E.Sc. degree in mechanical engineering, in 1987 and 1990, respectively and the Ph.D. degree in electrical engineering from the University of Western Ontario, London, ON, Canada, in 2002.

From 1990 to 1992, he held the position of Advanced Electrical Engineer in Engineering Research at 3M Canada Ltd., London, ON, Canada. From 1992 to 1993, he held the position of Senior Electronics Engineer in Machine Controls at Husky Injection Molding Systems, Bolton, ON, Canada. From 1993 to the present, he has been working at Siemens VDO Automotive Inc., London, ON, Canada, where he currently holds the position of Manager of Electronics Engineering. He was the responsible for the electronics design on the world's first brushless motor used for automotive engine cooling applications for which he received an innovation award from Siemens Canada Ltd. in 1997. His research interests include hardware and software design for motor drives and automotive electronics, EMC, as well as mechatronic systems simulation. He is the holder of six patents in the area of brush-motor and brushless-motor controls with several additional patents pending.

Joe LoVetri (S'87–M'90) was born in Enna, Italy, in 1963. He received the B.Sc. (with distinction) and M.Sc. degrees, both in electrical engineering, from the University of Manitoba, Winnipeg, MB, Canada, in 1984 and 1987, respectively, and the Ph.D. degree in electrical engineering from the University of Ottawa, Ottawa, ON, Canada in 1991.

From 1984 to 1986, he was an EMI/EMC Engineer at Sperry Defence Division, Winnipeg, MB, Canada. From 1986 to 1988, he held the position of TEMPEST Engineer at the Communications Security Establishment. Ottawa, ON, Canada. From 1988 to 1991, he was a Research Officer at the Institute for Information Technology of the National Research Council, Ottawa, ON, Canada. From 1991 to 1999, he was an Associate Professor in the Department of Electrical and Computer Engineering at The University of Western Ontario, London, ON, Canada. Between 1997–1998, he spent a sabbatical year at the TNO Physics and Electronics Laboratory, Den Haag, The Netherlands. He is currently with the Department of Electrical and Computer Engineering, University of Manitoba. His main interests lie in time-domain computational electromagnetics, modeling of electromagnetic compatibility problems, ground penetrating RADAR, and wideband identification techniques.